Model comparison of a VideoRay Pro 4 Underwater ROV

Simon Pedersen[1,2] Thomas Thuesen Enevoldsen[1] and Emil Már Einarsson[1]
[1] *Department of Energy Technology, Aalborg University Esbjerg, Niels Bohrs Vej 8, 6700 Esbjerg, Denmark.*
[2] *E-mail: spe@et.aau.dk*

***Abstract*—This study outlines a grey-box control-oriented model comparison of a VideoRay Pro 4 Underwater Inspection ROV with autonomous features. The respective models are developed and identified in previous studies and are based on three different model principles. The models are evaluated based on open-loop experimental tests with and without multiple thruster actuation. The tests show significant dynamic coupling between several motions, which none of the models estimate with sufficient accuracy without model extensions. Overall, it is concluded that all the three models are accurate in cases where the primary motions are directly actuated but also inaccurate when dynamic couplings exist.**

1. Introduction

Underwater robots are used in an increasing amount of tasks, such as mapping, surveillance, welding, inspections and assembly [1], [2]. The offshore industry is the biggest user of Remotely Operated Vehicles (ROVs) and Autonomous Underwater Vehicles (AUVs); mainly because of a significant decrease in operational cost over the last couple of years, see [3]. In general, most industrial ROV operations are manually controlled, with neither automatic control functions nor other autonomous capabilities [4]. However, automation has proven to decrease the time and cost of operation [5] and the inclusion of a precise model can be a significant part of the an automized control-strategy.

This paper will examine an industrial VideoRay Pro 4 ROV, which is commonly used for minor offshore inspection and maintenance tasks. The platform is versatile and handy due to the compact frame construction and relatively high acceleration. Several studies have focused on dynamic modeling of this ROV product for the purpose of model-based feedback control development [6], [7], [8], [9]. However, it is still an open discussion which model structure is preferable when model simplicity and accuracy are taken into account. This work will examine three different models, compare them to experimental data using the VideoRay Pro 4, and thus evaluate the pros and cons for the three considered models.

Figure 1. Photo of the VideoRay Pro 4 ROV with attached tether cable. There are three thrusters: One top thruster dedicated for heave, and two rear thrusters dedicated for surge and yaw.

TABLE 1. Available sensors and what they measure.

Sensors	Measurements	Units
Accelerometer	Linear acceleration	m/s^2
Gyroscope	Angular velocities	rad/s
Pressure sensor	Depth position	m
Compass	Heading angle	Rad
Temperature	External/Internal	^oC
Camera	Distance, heading and depth	-

2. VideoRay Pro 4

The considered vehicle is the VideoRay Pro 4 ROV, see figure 1. The electronics include a forward facing camera, a forward facing LED array and an inertial measurement unit, the available sensory information is shown in table 1. The ROV is powered by three thrusters, two rear-facing thrusters and one upward-facing thruster. The vehicle is rated for 300 m depths and has a maximum forward speed of approximately 2.1 m/s. It is powered through the tether and the controllers are running on the top-side computer. The current platform includes built-in PID controllers with the possibility of manually tuning using the VideoRay's graphical user interface. See [10] for further technical details.

3. Model Structures

In this section three different models of the ROV will be described, respectively. It should be noted that the

models' parameters are identified in existing literature; see [6], [11], [8], [9]. In figure 2 the forces applied to the ROV are illustrated; the purple boxes indicate the points where thruster forces are applied for the left, right and top thruster, respectively. The red sphere indicates the center of buoyancy (CB), and the green sphere indicates the center of mass (CM). The motions will be influenced by the external forces shown in table 2, which include force from the thrusters and various internal forces.

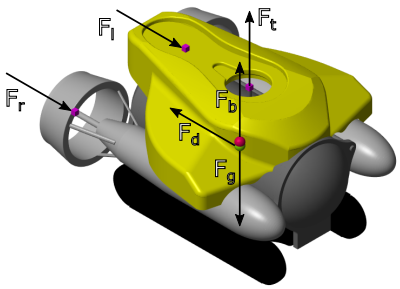

Figure 2. Visualization of the forces acting on the ROV

TABLE 2. Forces acting on the ROV body

Symbol	Description
$F_{(l,t,r)}, \tau_{(l,t,r)}$	Thruster forces of left, top and right thruster
F_d, τ_d	Drag force
F_g	Gravity force
F_b	Buoyancy force

Figure 3 shows the ROV with the 6 DOF in both body and world frame. A rotation matrix can be used for conversion between world and body frame using Euler Angle Transformation, see [12] for details. Here, the sway motion is neglected as there is no dedicated sway thruster installed on the considered prototype.

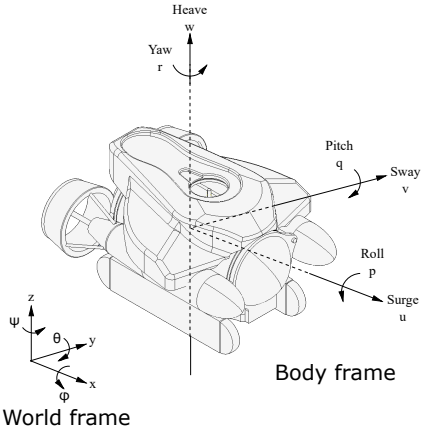

Figure 3. Reference frames and notations [8].

Since the comparison of the three models will be compared using the default thruster configuration (two rear, one top) some of the following models will be simplified accordingly. All of the models will be using the same input signals as excitations, and hence some minor modification of the models have been included in the following.

3.1. Model 1 [9] - Enevoldsen et al. (2018)

The model in [9] is based on the free-body diagram on figure 2, where the equations of motion are obtained describing the 3 directly controllable degrees of freedom, based on Newtons second law.

$$m_{rov}\dot{u} = F_r + F_l - F_d^u + f(r,q,p) \tag{1}$$

$$m_{rov}\dot{w} = F_t - F_d^w + g(r,q,p) \tag{2}$$

$$I_r\dot{r} = \tau_{rear} - \tau_d^r + h(q,p) \tag{3}$$

Here, neutral buoyancy is assumed; causing the gravitational and buoyancy forces to be insignificant due to cancellation. The functional expressions (f, g and h) added to the end of the movements contains the coupling dynamics between the given degrees of freedom. However, it is assumed that the ROV operates at low velocities, and thus the coupling dynamics are ignored. The torques described in equation (3) for the yaw movement are calculated by decomposing the thruster placements with respect to the center of mass, as shown in equation (4). γ is the angle for the rear thruster force vector decomposition. It is assumed that the rear thrusters during yaw motions receive an actuation signal of opposite signs to induce rotation.

$$I_r\dot{r} = R\sin(\gamma)(F_l + F_r) - (a_d r|r| + b_d r) \tag{4}$$

The model applies the same thrusters- and drag-to-force model structures found in [8], [13], and is shown in equation (21) and (22). The coefficients were identified from experiments.

The study also introduced tuning parameters, α and β, to improve the accuracy of the model [9]. The parameters are introduced as follows in equation (5), (6) and (7).

$$m_{rov}\dot{u} = \beta_u(\alpha_u(F_r + F_l) - F_d^u) \tag{5}$$

$$m_{rov}\dot{w} = \beta_w(\alpha_w F_t - F_d^w) \tag{6}$$

$$I_r\dot{r} = \beta_r(\alpha_r\tau_{rear} - \tau_d^r) \tag{7}$$

Modifying the parameter α impacts both the steady-state value and settling time, while scaling β only influences the settling time. A tuning guide was proposed [9].

This model includes few parameters in its simple structure, making them easy to identify experimentally. In order to compensate for the loss of accuracy due to simplicity, the tuning parameters are used to obtain a desired performance based on experimental data. Since there are only few model parameters, many of

the environmental-based characteristics are combined into single indistinguishable parameters. Hence, the environment in which the experiments for the parameter estimation takes place must reflect possible operation environments. Furthermore, this model is completely decoupled due to its simplicity. For further details regarding the model structure and the obtained physical parameters, see [9].

3.2. Model 2 [11] - Arnesen (2016)

This model is developed by [11] using the set physical parameters obtained in the work done by [6]. For detailed information about the model and the corresponding parameters estimation, see [6], [11]. The main equations applied in this model are derived from [12]:

$$\dot{\eta} = J(\psi)\nu \tag{8}$$

$$M\dot{\nu} = \tau - C(\nu)\nu - D(\nu)\nu - g(\eta) \tag{9}$$

Equation (8) and (9) are applied for an underwater vehicle that moves freely in surge, heave, yaw and sway, such that $M \in R^{4x4}$ is the rigid body and added mass inertial matrix (equation (10) and (11)), $C \in R^{4x4}$ is the rigid body and added mass terms due to coriolis and centrifugal forces (equation (12) and (13)), $D \in R^{4x4}$ contains damping force terms (equation (14) and (15)), $\tau \in R^{4x1}$ is the propulsion forces and $g(\eta)$ describe the restoration forces, where it is assumed that the roll and pitch are neutrally stabilizing.

$$M = M_{RB} + M_A \tag{10}$$

$$M = \begin{bmatrix} m + X_{\dot{u}} & 0 & 0 & 0 \\ 0 & m + Y_{\dot{v}} & 0 & 0 \\ 0 & 0 & m + Z_{\dot{w}} & 0 \\ 0 & 0 & 0 & I_z + N_{\dot{r}} \end{bmatrix} \tag{11}$$

$$C(\nu) = C_{RB}(\nu) + C_A(\nu) \tag{12}$$

$$C(\nu) = \begin{bmatrix} 0 & 0 & 0 & -mv + Y_{\dot{v}}v \\ 0 & 0 & 0 & mu - X_{\dot{u}}u \\ 0 & 0 & 0 & 0 \\ mv - Y_{\dot{v}}v & -mu + X_{\dot{u}}u & 0 & 0 \end{bmatrix} \tag{13}$$

The state vectors are represented by $\nu = [u, v, w, r]^T$ and $\eta = [x, y, z, \psi]^T$. The hydrodynamic damping can be divided into two terms: linear and quadratic damping,

$$D(\nu) = D_{lin} + D_{quad}(\nu) \tag{14}$$

$$D(\nu) = \begin{bmatrix} X_u + X_{|u|u}|u| & 0 & 0 & 0 \\ 0 & Y_v + Y_{|v|v}|v| & 0 & 0 \\ 0 & 0 & Z_w + Z_{|w|w}|w| & 0 \\ 0 & 0 & 0 & N_r + N_{|r|r}|r| \end{bmatrix} \tag{15}$$

and the restoration forces causing the roll and pitch states to naturally stabilize, such that

$$g(\eta) = [0\ 0\ \text{-}(W\text{-}B)\ 0\ 0\ 0]^T \tag{16}$$

where W is the force due to gravitational pull on the system and B is the buoyancy force.

3.2.1. Model modification. The original model introduced in [11] uses a 4-DOF model structure with a non-default thruster configuration, as an additional thruster is installed dedicated for sway movement. In this manuscript the sway thruster is neglected and the default thruster configuration (as in figure 2) is applied. Hence, the number of DOF's is reduced to 3, such that the state vectors now are represented by $\nu = [u, w, r]^T$ and $\eta = [x, z, \psi]^T$. This also means a reduction in the dimensions and removing the associated entries in the $C(\nu)$, M and $D(\nu)$ matrices, and the τ vector.

The model structure assumes that the input, τ, to the system is a propulsion force. Therefore, in order to perform the comparison a thrust-% to force relationship must be established. This relationship is chosen to be linear (see equation (17)), and tuned to the operating point of the other models.

$$\tau = \begin{bmatrix} F_l + F_r \\ F_t \\ \tau_{rear} \end{bmatrix} = \begin{bmatrix} G_1 & 0 & G_1 \\ 0 & G_2 & 0 \\ -G_3 & 0 & G_3 \end{bmatrix} \begin{bmatrix} u_l \\ u_t \\ u_r \end{bmatrix} \tag{17}$$

where G_x is the linear scaling factor tuned around the operating point and u is the input thruster percentage to the respective thrusters.

3.3. Model 3 [8] - Mai et al. (2017)

This section will describe the 6-DOF ROV model developed and identified in [8]. The model consists of a 3D CAD model where all included parameters were either measured or found in datasheets. Here, the buoyancy is calculated based on the total volume of the vehicle, see equation (18), and the gravity force is calculated using the total mass of the vehicle as shown in equation (19).

$$F_b = V_t \cdot \rho \cdot g \tag{18}$$

$$F_g = m_t \cdot g \tag{19}$$

where V_t is the total volume, m_t is the total mass, ρ is the density of the liquid, g is the gravitational constant. The thrust forces are mainly depending on two parameters; the propeller rotation speed, and the advance speed, as shown in equation (20).

$$\hat{F}_t(n, u_a) = \rho D^4 \left(\alpha_1 + \alpha_2 \frac{u_a}{nD}\right) n|n| \tag{20}$$

Where ρ is the fluid density, D is the propeller diameter, $\alpha_{1,2}$ are the propeller coefficient n is the propeller rotation speed and u_a is the advance speed. Assuming a linear relationship between the thruster rotation speed and control input $n = a \cdot u$, and by neglecting the influence of the advance speed, the thruster force can be modeled as a quadratic equation to the normalized control input u, shown in equation (21) [14], [13].

$$F_t(u_l, u_t, u_r) = \begin{bmatrix} T_l^l & 0 & 0 \\ 0 & T_l^t & 0 \\ 0 & 0 & T_l^r \end{bmatrix} \begin{bmatrix} u_l \\ u_t \\ u_r \end{bmatrix} + \begin{bmatrix} T_q^l & 0 & 0 \\ 0 & T_q^t & 0 \\ 0 & 0 & T_q^r \end{bmatrix} \begin{bmatrix} u_l^2 \\ u_t^2 \\ u_r^2 \end{bmatrix} \tag{21}$$

Where $u_{(l,t,r)}$ are the thruster input signals normalized to ± 1 and T are the thruster coefficients. The drag forces act against the current velocity of the vehicle, and is applied at the center of mass $\boldsymbol{CM}$. Here, the drag forces are modeled as an algebraic quadratic expressions, see equation (22) [14], [13].

$$F_d(u,v,w) = \begin{bmatrix} D_l^u & 0 & 0 \\ 0 & D_l^v & 0 \\ 0 & 0 & D_l^w \end{bmatrix} \begin{bmatrix} u \\ v \\ w \end{bmatrix} + \begin{bmatrix} D_q^u & 0 & 0 \\ 0 & D_q^v & 0 \\ 0 & 0 & D_q^w \end{bmatrix} \begin{bmatrix} u^2 \\ v^2 \\ w^2 \end{bmatrix} \tag{22}$$

where u, w, v are the cartesian velocities.

The drag coefficients have been calculated such that the the drag at maximum velocity equals the thruster force as shown in equation (23). Furthermore, for any other velocity the linear to quadratic ratio drag is maintained as shown in equation (24).

$$F_l(1) + F_r(1) = D_u^q \cdot u_{max}^2 + D_u^l \cdot u_{max} \tag{23}$$

$$\frac{D_u^q}{D_u^l} = C \tag{24}$$

The drag ratio C is calculated given the numbers from [13] ($C = 0.16$). For the rotational drags, the coefficients from [13] have been applied. The center of mass was calculated based on the operation in equation (26) because the parts are rigidly constrained to each other.

$$m_t = \sum \vec{M}_p \tag{25}$$

$$C\vec{M} = \vec{M}_p \cdot \vec{p_p} \cdot \frac{1}{m_t} \tag{26}$$

where $\vec{M}_p$ is the vector of component masses, p_p is the offset, m_t is the total mass. Similarly, the center of buoyancy ($\boldsymbol{CB}$) can be found using the volumes of the bodies as shown in equation (28).

$$V_t = \sum \vec{V}_p \tag{27}$$

$$C\vec{B} = \vec{V}_p \cdot \vec{p_p} \cdot \frac{1}{V_t} \tag{28}$$

The center of gravity and mass are identical in the x- and y-axes, whereas there is a difference of 5.59 mm in the z axes. This corresponds well to the self-righting behavior in the roll and pitch, similar to what is assumed in section 3.2.

Since the model parameters are obtained with the application of a 3D model, the model allows for the inclusion of advanced features from the physical structure of the ROV. This is beneficial for determining parameters associated with the given degrees of freedom, especially for the drag force parameters since the shape of the hull is taken into consideration. This model structure also includes the coupling between the motions. One downside of this approach is that it requires an accurate 3D CAD model of the vehicle of choice in order to reflect the system characteristics and thus requires a more extensive simulation implementation where the model accuracy is given a higher priority than model simplicity. For detailed information of the model, see [8].

4. Model comparison

In this section the three models examined in section 3 will be compared to open-loop experimental data.

The model comparisons are based on both single and multiple DOF dedicated actuation. In all test scenarios two independent experiments (marked blue and light blue) are carried out to show potential uncertainties in the disturbances from the tether and underwater streams, and other running condition variations. The input thrust (marked red) is shown for both the depth (top thruster) and heading (the rear thrusters), while the three models output responses (marked purple for model 1, green for model 2, and black for model 3) are plotted for comparison with each other and the experiments. For the investigation of the dynamic coupling only model 3 is included as it is the only model where any coupling is nonzero.

4.1. Single DOF actuation

In this section only single DOF actuation is used for the heave motion (figure 4 and 5) and yaw motion (figure 6 and 7). All the tests are based on input steps of sizes between 30 % and 90 % thruster percentage in both directions in turns. Figure 4 shows a comparison

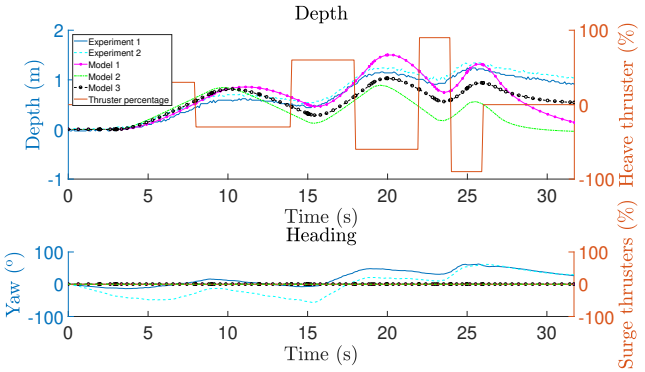

Figure 4. Depth and heading at 30%, 60% and 90% thrust in the top thruster.

between the 3 models and two experiments when the heave thruster is given 30%, 60% and then 90% thrust in both directions. The ROV clearly drifts in depths since the thruster provides more force in one direction due to the thruster's physical shape and propeller design. Besides the drifting, all three models have an acceptable accuracy although they all simulate a larger heave motion than the experiments show causing minor deviation to the experiments which obviously adds up over time. The ROV also has a small movement in the yaw direction, which is mainly caused by the tether acting on

the ROV. As the tether is not included as a disturbance to any of the models, none of the models capture the yaw motion. Figure 5 shows the coupling of pitching and

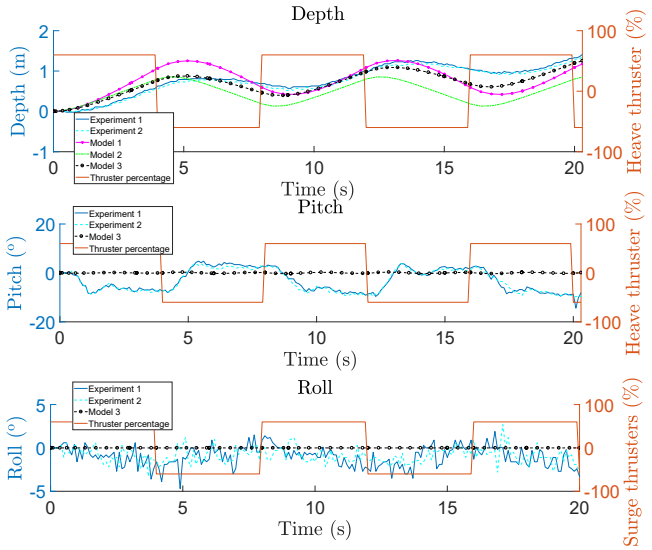

Figure 5. Depth, pitch and roll at 60% thrust in the top thrusters.

roll to ±60% heave thrust, which none of the models sufficiently capture although they are accurate for the main motion (depth). The ROV goes to +5 deg when heaving upwards and down to −10 deg when heaving downwards, which is a significant difference. However, model 3 completely under-estimates this coupling. There is also a tendency of a minor roll motion during negative heave velocity, but model 3 does not capture this either. Figure 6 shows the depth and heading at 30%, 60% and

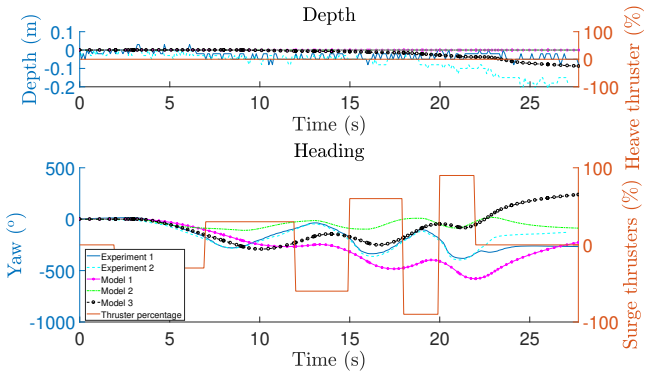

Figure 6. Depth and heading at 30%, 60% and 90% thrust in the rear thrusters.

then 90% thrust in the yaw movement. The depth is not affected when only using yaw. One of the experiments show some drifting in the depth, but it is caused by the tether getting entangled somewhat during the ROV rotations. All models estimate the yawing to an acceptable level, although model 1's yaw response is reacting slower on the input step changes than both the experiments and the two other models. Figure 7 shows the rear

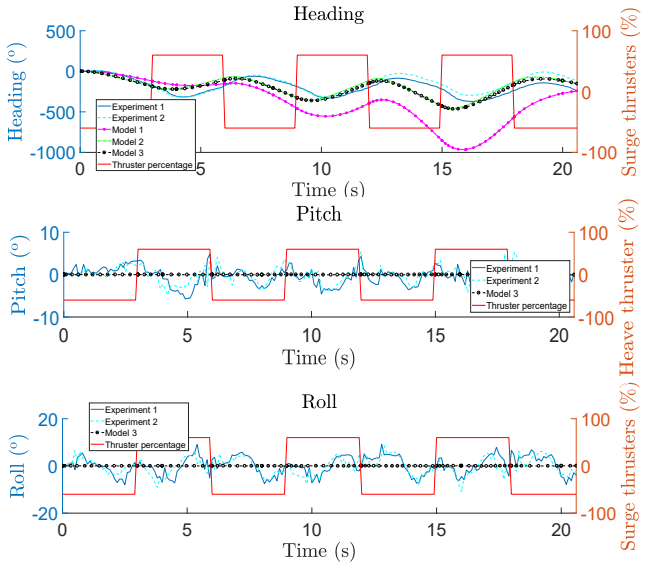

Figure 7. Heading, pitch and roll at 60% thrust in the rear thrusters.

thrusters actuation effect on the rolling and pitching. Both have oscillating movements when actuated by the yaw thrusters. The roll peaks at −10 and +10 deg which is an essential effect not captured by model 1 and 2, and under-estimated by model 3. A similar tendency is observed for the pitching. As the ROV has a small mass it is sensitive to disturbances when yawing, where especially the tether impacts pitching and rolling. Thus, it is possible that the accuracy of the models are limited by the model structures and can be improved by adding the attached tether physics.

4.2. Multiple DOF actuation

In this section all three thrusters act at the same time, primarily causing a yaw and heave motion at the same time. Figure 8 and 9 show time responses from the same data set where all three thrusters are actuated in steps in different time intervals. Figure 9 shows similar behavior as in figure 7, where model 1 is deviating the most from the experiments, and some roll fluctuations occur which only model 3 capture, but with a bad estimation. Hence, the top thruster and the heave motion in general does not influence the heading much. However, in Figure 8 it is clear from the experiments that the thrusters impact the pitching significantly. None of the models estimates this. The pitching angle increases from the ones seen in figure 5 where only the top thruster is actuated, and none of the models estimate this well. Overall, this experiment shows a high coupling between the motions which none of the models can capture with sufficient accuracy.

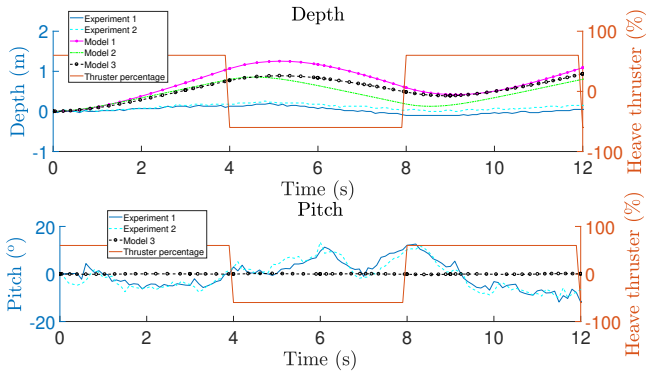

Figure 8. Depth and pitch at 60% thrust for both the top and rear thrusters.

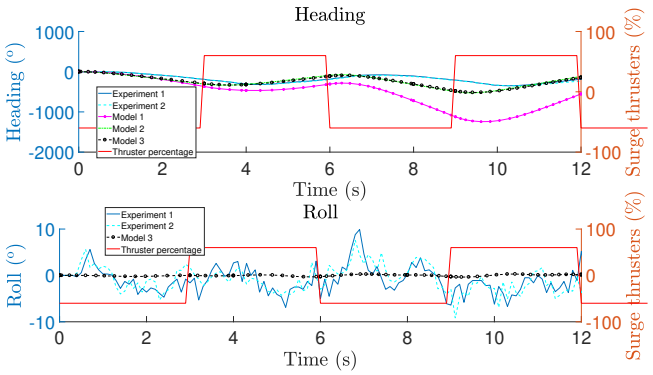

Figure 9. Heading and roll at 60% thrust for both the top and rear thrusters. Same experiment as in Figure 8.

5. Conclusion and future work

In this work three different dynamic models of a commercial VideoRay Pro 4 Underwater ROV are compared with data from open-loop experiments. The considered models are developed and identified in existing work [6], [11], [8], [9], and thus this study's only model modifications are unit conversions such that the three models directly can be compared to the obtained data. It is clear that all the models potentially can be accurate for heading and heaving when they are the primary motions actuated by the top and rear thrusters, respectively. However, for the coupling between the motions all three models are inaccurate; model 1 and 2 do not have any coupling introduced due to the simplified physics the models are based on, and model 3 under-estimates them in all the investigated cases. Furthermore, the attached tether also impacts the results and all three models could benefit with the addition of a tether model.

The overall conclusion is that each of the three models can be used as a framework for controller development as they all have simple model structures, are easy to identify and have decent accuracies in most scenarios. Model 2 and 3 have a better accuracy, while model 1 and 2 have simpler model structures than model 3. However, at larger thruster actuation the couplings are more dominant and thus an inclusion or retuning of the coupling dynamics can potentially improve the overall accuracy for all three models in these operational regions.

References

[1] C. Mai, S. Pedersen, L. Hansen, K. L. Jepsen, and Z. Yang, "Subsea infrastructure inspection: A review study," in *2016 IEEE International Conference on Underwater System Technology: Theory and Applications (USYS)*, Dec 2016, pp. 71–76.

[2] R. B. Wynn, V. A. Huvenne, T. P. L. Bas, B. J. Murton, D. P. Connelly, B. J. Bett, H. A. Ruhl, K. J. Morris, J. Peakall, D. R. Parsons, E. J. Sumner, S. E. Darby, R. M. Dorrell, and J. E. Hunt, "Autonomous Underwater Vehicles (AUVs): Their past, present and future contributions to the advancement of marine geoscience," *Marine Geology*, vol. 352, pp. 451 – 468, 2014.

[3] A. Reid, "ROV Market Prospects," 2013. [Online]. Available: http://www.subseauk.com/documents/presentations/ssuk%20-%20rov%20event%20-%20sep%202013%20%5Bweb%5D.pdf

[4] I. Schjoelberg and I. B. Utne, "Towards autonomy in rov operations," *IFAC-PapersOnLine*, vol. 48, no. 2, pp. 183 – 188, 2015.

[5] I. Tena, "Automating ROV Operations in aid of the Oil & Gas Offshore Industry," 2011.

[6] O. A. Eidsvik, "Identification of hydrodynamic parameters for remotely operated vehicles," Master's thesis, NTNU, 2015.

[7] B. O. Arnesen, A. M. Lekkas, and I. Schjoelberg, "3D Path Following and Tracking for an Inspection Class ROV," *ASME 36th International Conference on Ocean, Offshore and Arctic Engineering*, vol. 7a, no. OMAE2017-61170, p. V07AT06A019, 2017.

[8] C. Mai, S. Pedersen, L. Hansen, K. L. Jepsen, and Z. Yang, "Modeling and Control of Industrial ROV's for Semi-Autonomous Subsea Maintenance Services," *IFAC Congress*, 2017.

[9] T. T. Enevoldsen, E. M. Einarsson, S. Pedersen, and Z. Yang, "Simplified Modelling and Identification of an Inspection ROV (To be published)," in *3rd IFAC Workshop on Automatic Control in Offshore Oil and Gas Production (OOGP)*, May 2018.

[10] VideoRay LCC, "VideoRay Pro 4 Operation Manual," 2012. [Online]. Available: http://www.videoray.com/images/User_Manuals/pro_4_manual.pdf

[11] B. O. Arnesen, "Motion control systems for rovs-underwater path-following for a videoray pro 4 rov," Master's thesis, NTNU, 2016.

[12] T. I. Fossen, *Handbook of marine craft hydrodynamics and motion control.* John Wiley and Sons, 2011.

[13] W. Wang and C. M. Clark, "Modeling and Simulation of the VideoRay Pro III Underwater Vehicle," *IEEE OCEANS 2006*, 2006.

[14] M. Blanke, "Ship Propulsion Losses Related to Automated Steering and Prime Mover Control," *PhD thesis, The Technical University of Denmark, Lyngby*, 1981.